Quasiparticle scattering interference in superconducting iron pnictides

Yan-Yang Zhang,[1] Chen Fang,[1] Xiaoting Zhou,[1] Kangjun Seo,[1] Wei-Feng Tsai,[1] B. Andrei Bernevig,[2] and Jiangping Hu[1]
[1]*Department of Physics, Purdue University, West Lafayette, Indiana 47907, USA*
[2]*Princeton Center for Theoretical Science, Princeton University, Princeton, New Jersey 08544, USA*
(Received 14 March 2009; revised manuscript received 30 August 2009; published 29 September 2009)

Using both two orbital and five orbital models, we investigate the quasiparticle interference (QPI) patterns in the superconducting (SC) state of iron-based superconductors. We compare the results for nonmagnetic and magnetic impurities in sign-changed s-wave $\cos(k_x)\cdot\cos(k_y)$ and sign-unchanged $|\cos(k_x)\cdot\cos(k_y)|$ SC states. While the patterns strongly depend on the chosen band structure details, the sensitivity of peaks around $(\pm\pi,0)$ and $(0,\pm\pi)$ wave vectors on magnetic or nonmagnetic impurities, and on sign-changed or sign-unchanged SC orders is a common feature. Our results suggest that the QPI can provide evidence of the pairing symmetry in the SC states.

DOI: 10.1103/PhysRevB.80.094528 PACS number(s): 74.25.Jb, 74.20.−z

I. INTRODUCTION

Recently, the discovery of high-temperature superconductivity in oxypnictide compounds[1–5] stirred great interests in the condensed matter community. One important problem is to elucidate the pairing symmetry of the order parameter of the superconducting (SC) state. Theoretically many possible gap pairing symmetries have been proposed. Due to the proximity of the superconducting state to a collinear antiferromagnetic state, a magnetism-based mechanism has emerged in both the weak and strong coupling approaches. This mechanism suggests that an extended s-wave pairing symmetry is favored.[6–8]

The weak-coupling approach favors an s-wave (so-called $s_{\pm}$) state[7] in which the relative sign of order parameters changes between the hole and electron pockets. However, the weak-coupling approach does not specify the exact form of order parameter. In a recent paper,[6] we showed that, in strong coupling, the pairing symmetry is determined mainly by the next nearest neighbor antiferromagnetic exchange coupling J_2 (Refs. 9–13) and has an explicit $s_{x^2y^2}$ form in momentum space, $\cos(k_x)\cdot\cos(k_y)$. This result is completely independent of any model, *as long as* the dominating interaction is next-nearest neighbor J_2 *and* the Fermi surfaces (FSs) are located close to the Γ and M points in the Brillouin zone. The $\cos(k_x)\cdot\cos(k_y)$ changes sign between the electron and hole pockets in the Brillouin zone. In this sense, it resembles the order parameter, $s_{\pm}$, proposed through general weak-coupling arguments.[7]

The magnitudes of superconducting gaps measured by angle-resolved photoemission spectroscopy on different Fermi surfaces are in good agreement with the simple $\cos(k_x)\cdot\cos(k_y)$.[14–16] The magnetic properties in the SC state have also been shown to be consistent with the proposed pairing symmetry.[17–20] Although several theoretical works[21–24] propose different ways to measure the sign change between the electron and hole pockets, directly probing this change is still a fundamental experimental challenge. Without any detailed calculations, a theoretical suggestion for probing the sign change through quasiparticle interference (QPI) in the presence of magnetic and nonmagnetic impurities. has been made in Ref. 25.

The QPI can be probed directly in modern scanning tunnel microscopy experiments[26,27] and has been intensively studied in copper-based high-temperature superconductors. In the presence of impurities, elastic scattering mixes two eigenstates with different momentum $\mathbf{k}_1$ and $\mathbf{k}_2$ on the same contour of constant energy and a scattering interference pattern appears as a modulation in the local density states (LDOS) at wave vector $\mathbf{q}=\mathbf{k}_2-\mathbf{k}_1$. Such kind of interference pattern in the wave-vector space can be observed in the Fourier transform scanning tunneling spectroscopy (FT-STS).[28,29] The quasiparticle scattering between regions in the $\mathbf{k}$ space produces peaks or arcs determined by high density of states (DOS) in momentum space and coherence factors.[30] For example, in the d-wave pairing SC state, many QPI dispersive peaks can be identified; in the cuprates, they provide details of the band structure, the nature of superconducting gap or other competing orders.[31–43]

In this paper, we perform a detailed investigation of the QPI in iron-based superconductors. We use both two orbital and five orbital models. In general, the QPI strongly depends on the bare band structure. The QPI patterns change significantly from a two orbital model to a five-orbital one, which suggests that the QPI can provide direct information of the detailed band structure and orbital degrees of freedom. By carefully examining the pattern, we can also identify common features of the QPI pattern in both models, which are tied to the symmetry of SC order parameter and the impurity type. These general features include: (1) the intraorbital scattering by impurities always dominates the interorbital scattering. The latter has negligible effect on the QPI (though it breaks discrete C_4 symmetry of the patterns); (2) unlike in the d-wave SC state of cuprates where large density of states at some banana tips causes dispersive features in the QPI,[28] the nodeless s-wave has little density of states inside SC gaps and hence no strong points dominate the scattering; (3) a magnetic impurity always causes a broad and large peak near $\mathbf{q}=(0,0)$ in the QPI; this stems from intraband scattering. For a nonmagnetic impurity, the intensity around $\mathbf{q}=(0,0)$ is small. This result can be used to distinguish two types of impurities; and (4) the peaks around $(\pm\pi,0)$ and $(0,\pm\pi)$ are sensitive to both the type of impurities and to the sign change of the SC orders between the electron and hole pockets. Magnetic impurities along with sign-unchanged SC or-

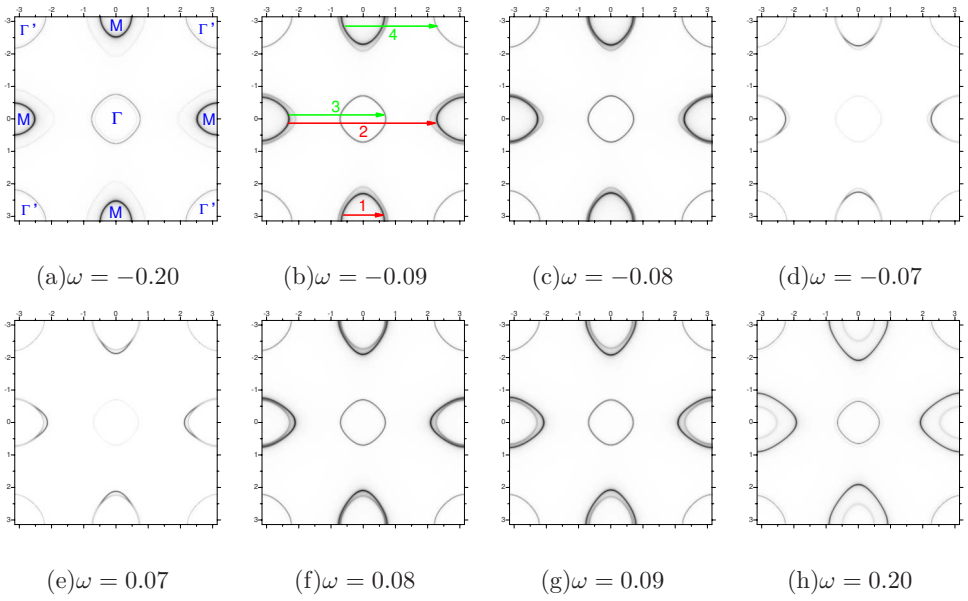

FIG. 1. (Color online) The spectral function $\mathcal{A}(\mathbf{k},\omega)$ in the unfolded Brillioun zone, for $s_{x^2y^2}$ with Δ_0=0.1. Darker regions correspond to larger values of $\mathcal{A}$ hence larger DOS in $\mathbf{k}$ space.

ders or nonmagnetic impurity with sign-changed SC orders cause strong interference peaks. Finally, as in a fully-gapped *s*-wave SC state the results from a full *T*-matrix calculation do not differ considerably from results of a simple first order perturbation calculation,[30,44] we are able to also provide an analytic derivation of the above results.

II. TWO-ORBITAL MODEL AND SINGLE IMPURITY SCATTERING

We first investigate the QPI in a simple two orbital model.[6,17,45] The mean field Hamiltonian of the model in SC states is written as $H=\Sigma_{\mathbf{k}}\Psi^{\dagger}(\mathbf{k})B(\mathbf{k})\Psi(\mathbf{k})$ with

$$B(\mathbf{k})=\begin{pmatrix} \epsilon_x(\mathbf{k})-\mu & \Delta_1(\mathbf{k}) & \epsilon_{xy}(\mathbf{k}) & 0 \\ \Delta_1^*(\mathbf{k}) & -\epsilon_x(\mathbf{k})+\mu & 0 & -\epsilon_{xy}(\mathbf{k}) \\ \epsilon_{xy}(\mathbf{k}) & 0 & \epsilon_y(\mathbf{k})-\mu & \Delta_2(\mathbf{k}) \\ 0 & -\epsilon_{xy}(\mathbf{k}) & \Delta_2^*(\mathbf{k}) & -\epsilon_y(\mathbf{k})+\mu \end{pmatrix}, \tag{1}$$

where $\Psi^{\dagger}(\mathbf{k})=(c^{\dagger}_{1,\mathbf{k},\uparrow},c_{1,-\mathbf{k},\downarrow},c^{\dagger}_{2,\mathbf{k},\uparrow},c_{2,-\mathbf{k},\downarrow})$ in the Nambu formalism. The single-particle bands read as

$$\epsilon_x(k_x,k_y)=-2t_1\cos k_x-2t_2\cos k_y-4t_3\cos k_x\cos k_y,$$

$$\epsilon_y(k_x,k_y)=\epsilon_x(k_y,k_x),\quad \epsilon_{xy}(k_x,k_y)=-4t_4\sin k_x\sin k_y,$$

where t_1=−1, t_2=1.3, t_3=t_4=−0.85, and μ is chosen in the electron-doped regime. By comparing with the DFT results in the low energy, the absolute value of t_1 is estimated as ~0.3 eV.[46,47] Hereafter, $|t_1|$ will be used as the energy unit. For $s_{x^2y^2}$-wave pairing, the order parameter is $\Delta_1(k_x,k_y)=\Delta_2(k_x,k_y)=\Delta_0\cos k_x\cos k_y$.[6,17]

The Green's function for the clean system is

$$G^0(\mathbf{k},\omega)\equiv G^0(\mathbf{k},\mathbf{k},\omega)=[(\omega+i\delta)I-B(\mathbf{k})]^{-1}, \tag{2}$$

where I is the identity matrix and δ is the energy width broadening. In this work, we only consider a single impurity with potential $\sim\delta(\mathbf{x})$ so that the impurity matrix $V(\mathbf{k}_1,\mathbf{k}_2)=V$ is independent of $\mathbf{k}$. The impurity induced Green's function is expressed as

$$\delta G(\mathbf{k}_1,\mathbf{k}_2,\omega)=G^0(\mathbf{k}_1,\omega)T(\mathbf{k}_1,\mathbf{k}_2,\omega)G^0(\mathbf{k}_2,\omega). \tag{3}$$

Standard perturbation theory gives

$$\begin{aligned} T(\omega)&=V+V\Gamma^0(\omega)V+V\Gamma^0(\omega)V\Gamma^0(\omega)V+\cdots \\ &=[I-V\Gamma^0(\omega)]^{-1}V, \end{aligned} \tag{4}$$

where

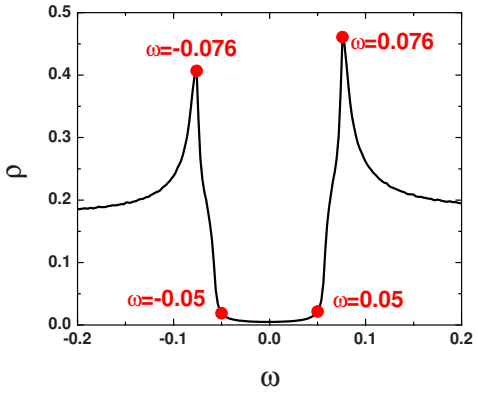

FIG. 2. (Color online) Bulk density of states ρ for $s_{x^2y^2}$ as a function of ω, Δ_0=0.1 and no impurities. Some special values are marked by red dots. The energy broadening width is δ=0.002.

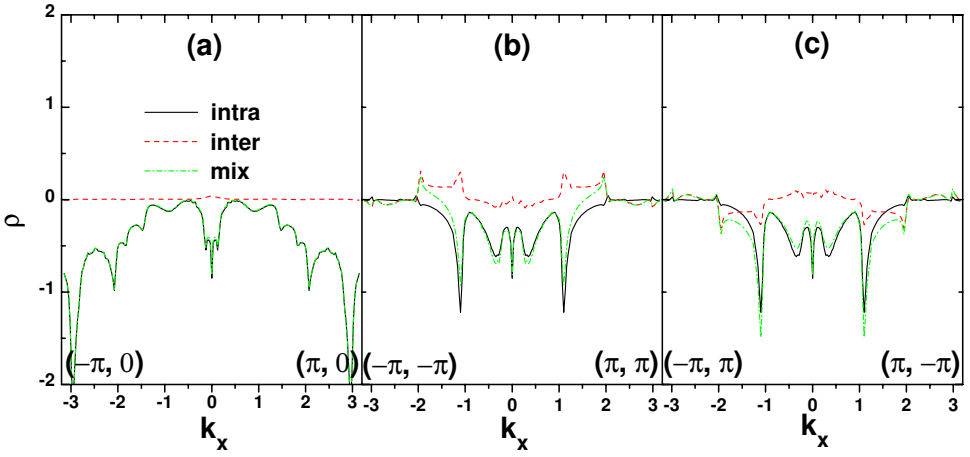

FIG. 3. (Color online) $\delta\rho(\mathbf{q},\omega=0.07)$ for nonmagnetic impurity with V_{intra} (black solid), V_{inter} (red dash) and $V_{\text{mix}}\equiv V_{\text{intra}}+V_{\text{inter}}$ (green dash dot) along three directions: (a) $(-\pi,0)\rightarrow(\pi,0)$, (b) $(-\pi,-\pi)\rightarrow(\pi,\pi)$, and (c) $(-\pi,\pi)\rightarrow(\pi,-\pi)$.

$$\Gamma^0(\omega)=\int\frac{d^2k}{(2\pi)^2}G^0(\mathbf{k},\omega). \tag{5}$$

Consequently, the Fourier transform of the (induced) local density of states is

$$\delta\rho(\mathbf{q},\omega)=\frac{i}{2\pi}\int\frac{d^2k}{(2\pi)^2}g(\mathbf{k},\mathbf{q},\omega), \tag{6}$$

where $\mathbf{q}=\mathbf{k}'-\mathbf{k}$ and

$$g(\mathbf{k},\mathbf{q},\omega)=\delta G_{11}(\mathbf{k},\mathbf{k}',\omega)-\delta G_{11}^*(\mathbf{k}',\mathbf{k},\omega)+\delta G_{33}(\mathbf{k},\mathbf{k}',\omega)-\delta G_{33}^*(\mathbf{k}',\mathbf{k},\omega). \tag{7}$$

Due to the multiorbital nature of the band model, we distinguish different types of impurities. They are

$$V=V_{\text{intra}}=I\otimes\begin{pmatrix}V_0 & 0\\ 0 & \pm V_0\end{pmatrix}, \tag{8}$$

for an impurity with only intraorbital scattering, and

$$V=V_{\text{inter}}=\sigma_x\otimes\begin{pmatrix}V_0 & 0\\ 0 & \pm V_0\end{pmatrix}, \tag{9}$$

for interorbital scattering only, where the upper (down) sign corresponds to magnetic (nonmagnetic) impurity. Since it was argued that for cuprate superconductors this T-matrix method is valid when impurity scattering strength is much larger than the maximal pairing gap,[27] we take $V_0=4\Delta_0$ in our calculation. Our following results weakly depend on V_0 as long as $VN_0\ll 1$.

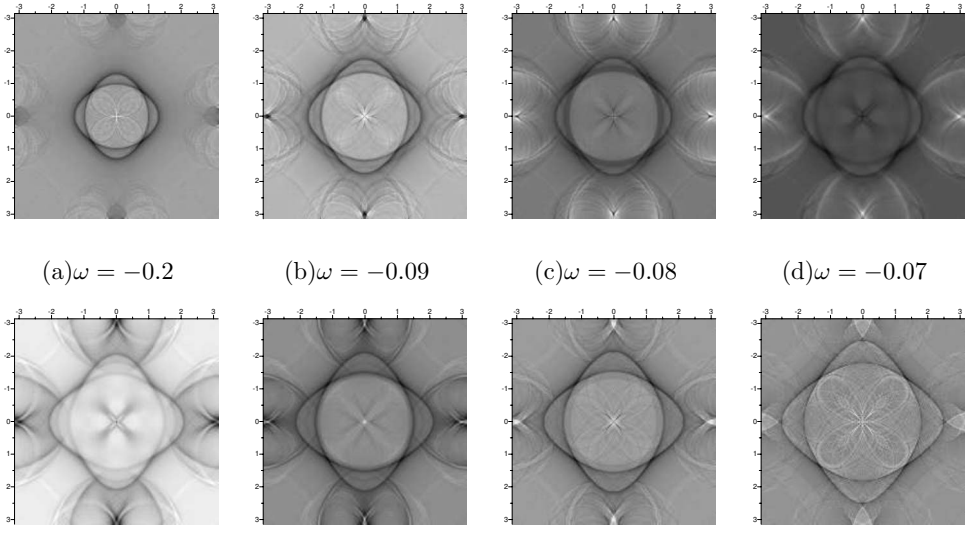

FIG. 4. $\delta\rho(\mathbf{q})$ for nonmagnetic impurity with intraorbital scattering, $V_0=0.4$. A 200×200 lattice in $\mathbf{k}$-space is used in numerical integration of Eq. (5) and the energy broadening width $\delta=0.005$.

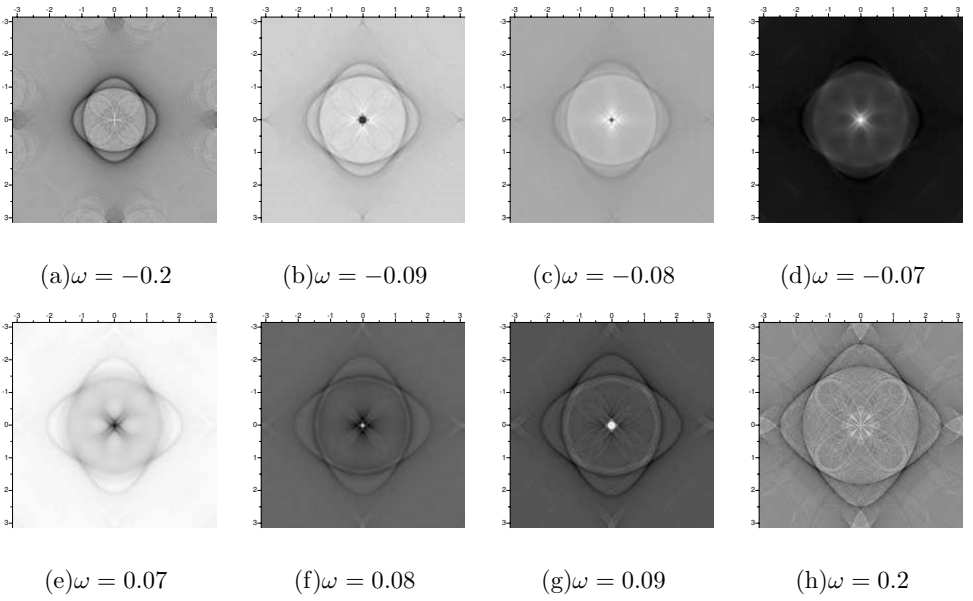

FIG. 5. The same with Fig. 4 but for magnetic impurity, V_0=0.4.

A. Numerical results

We first calculate electronic properties in an impurity-free system. Most of the results in this section have been already computed in less detail in Ref. 17. In Fig. 1, we plot the spectral function

$$\mathcal{A}(\mathbf{k},\omega) = -\frac{1}{\pi}\mathrm{Im}[G^0_{11}(\mathbf{k},\omega) + G^0_{33}(\mathbf{k},\omega)] \qquad (10)$$

of the clean system at different ω in the unfolded Brillioun zone. This unfolded Brillioun and the typical value of order parameter Δ_0=0.1 will be used throughout this paper. It should be noted that for ω and $-\omega$, the shapes (topology) of the contours of constant energy (CCE) are almost identical, but the numerical values of $\mathcal{A}$ on these contours are remarkably different. As an example, let us focus on the regions near one of the M points $(\pi,0)$, where the CCE consists of two semi-oval circles, or two complete oval circles due to the periodicity of the Brillioun zone (BZ). As can be seen from Figs. 1(a) and 1(b), for negative ω, the spectral weight on the inner circle is larger than that on the outer one. The situation is opposite for positive ω [Figs. 1(g) and 1(h)]. This leads to different scattering interference patterns at $\pm\omega$, as we will see later on.

The bulk density of states $\rho(\omega)=\Sigma_{\mathbf{k}}\mathcal{A}(\mathbf{k},\omega)$ is plotted in Fig. 2. It is fully gaped within $\sim(-0.05,0.05)$ and the coherent peak occurs at $\sim\pm0.076$.[17] To exemplify some scattering amplitudes, we plot $\delta\rho(\mathbf{q})$ for a nonmagnetic impurity near the edge of the gap (ω=0.07) along three special directions in Fig. 3. Two observations in these figures are common to all our results. First, $\rho(\mathbf{q})$ for interorbital scattering in the two diagonal directions are quite different ([compare the red dash lines in Figs. 3(b) and 3(c)]. This is not surprising since the interorbital scattering such as $c^\dagger_{1,\mathbf{k},\uparrow}c_{2,\mathbf{k},\uparrow}$ breaks the symmetry between directions $(-\pi,-\pi)\rightarrow(\pi,\pi)$ and $(-\pi,\pi)\rightarrow(\pi,-\pi)$.[48] Second, the amplitude created by the intraorbital impurity is stronger than that created by the interorbital one;

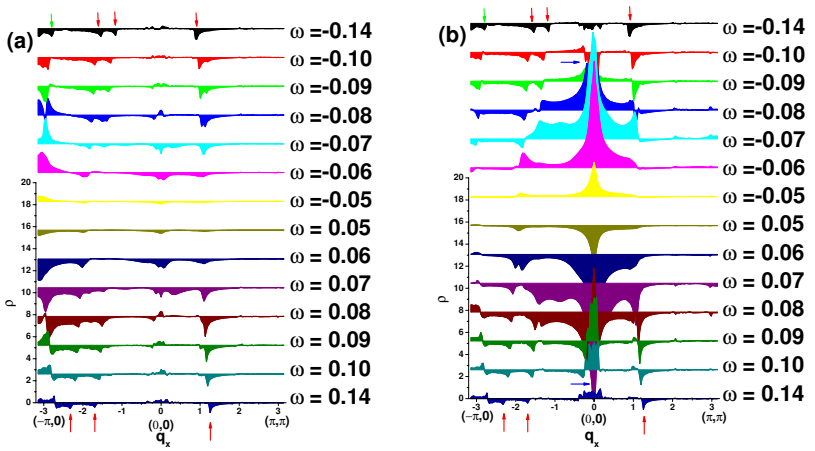

FIG. 6. (Color online) Profiles of $\delta\rho(\mathbf{q},\omega)$ along $\mathrm{M}\rightarrow\Gamma\rightarrow\Gamma'$ for (a) nonmagnetic impurity and (b) magnetic impurity. The data are shifted vertically relative to each other for clarity.

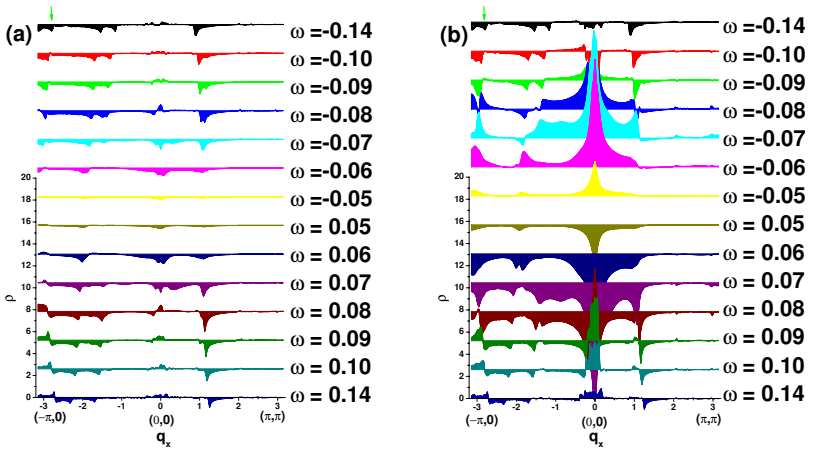

FIG. 7. (Color online) Same as Fig. 6 but for the case without sign change, $\Delta_1(k_x,k_y)=\Delta_2(k_x,k_y)=|\Delta_0 \cos k_x \cos k_y|$. (a) Nonmagnetic impurity and (b) magnetic impurity.

therefore the intraorbital scattering is dominant when both are present. As such, in the following, we present only numerical results for intraorbital impurities.

In Figs. 4 and 5, we show the two-dimensional contour of the scattering pattern $\delta\rho(\mathbf{q})$ for nonmagnetic and magnetic impurities, respectively. The $\delta\rho(\mathbf{q})$ profiles along special directions are plotted in Fig. 6. In Figs. 4 and 5, the most prominent features for all ω values are two intersecting ovals [see also the peaks directed by red arrows (1 and 2) in Fig. 6], reflecting the strong intrapocket scattering between equal-energy curves near M points with the largest DOS. These scattering processes are labeled by red arrows (1 and 2) in Fig. 1(b), where scattering wave vectors outside the first BZ (e.g., arrow 2) should be understood as their equivalent counterparts in the first BZ. By increasing $|\omega|$ on the negative (positive) energy side, the size of the ovals decreases (increases) because the important scattering takes place between the inner (outer) circle of CCE near M with the largest

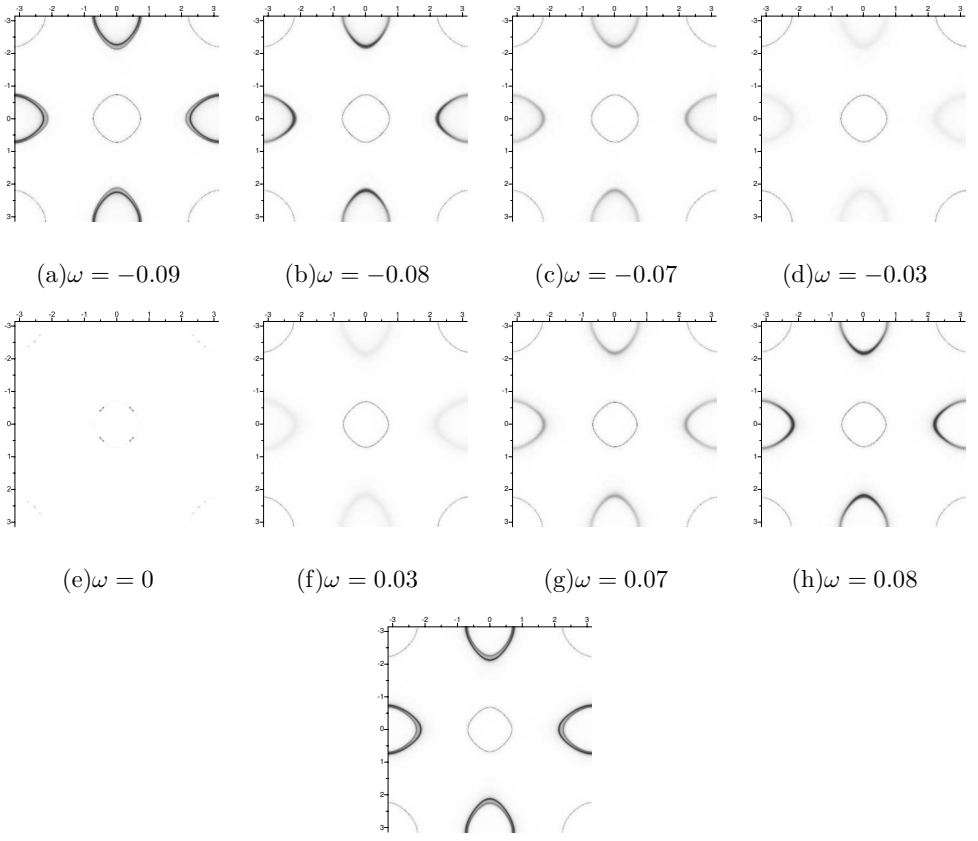

FIG. 8. The spectral function $\mathcal{A}(\mathbf{k},\omega)$ for $d_{x^2-y^2}$ pairing symmetry with Δ_0=0.1.

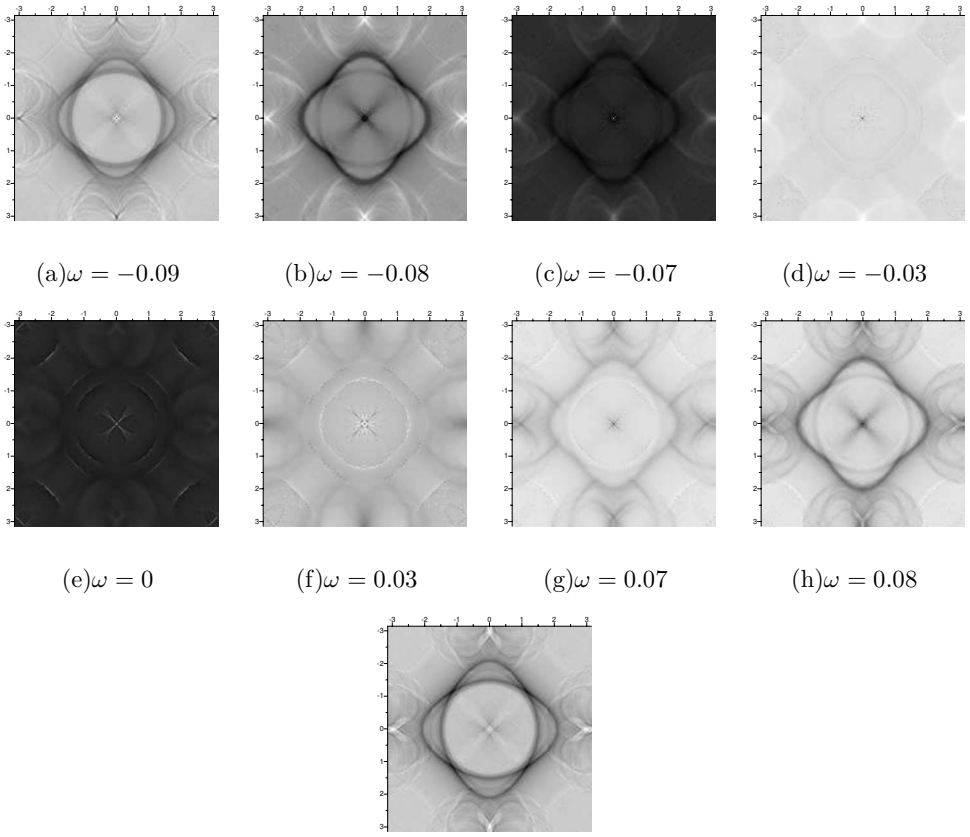

FIG. 9. $\delta\rho(\mathbf{q})$ for nonmagnetic impurity for $d_{x^2-y^2}$ pairing symmetry with intraorbital scattering, $V_0=0.4$.

DOS. At a definite energy ω, this gives two peaks along direction $M\rightarrow\Gamma$, corresponding to the scattering along the major and minor axis of the oval CCE, respectively. Due to the congruence of these CCE oval circles, they always intersect on the diagonal line $(\Gamma'\rightarrow\Gamma)$, therefore only one peak can be observed along this direction. For ω far outside the gap, there is no noticeable difference between the magnetic and nonmagnetic impurities [compare Figs. 4(a) and 4(h) with Figs. 5(a) and 5(h)]. This is understandable since the tendency of the (Cooper) pair breaking due to a magnetic impurity is most significant near the Fermi level. Within the single-particle scattering regime considered here, for $|\omega|<0.05$ inside the gap, no interference pattern is expected due to lack of scattering states. This is confirmed (but not shown here) by the fact that, when decreasing the imaginary part of the energy δ in Green's functions, the peaks of $\delta\rho(\mathbf{q},|\omega|>0.05)$ are sharper, while $\delta\rho(\mathbf{q},|\omega|<0.05)$ vanishes trivially for all $\mathbf{q}$.

There are additional peaks around the M points, as directed by green arrows in Fig. 6, which play an important role in distinguishing different types of impurities. When decreasing $|\omega|$, they move steadily toward M. These originate from the interpocket scattering as demonstrated by green arrows (3 and 4) in Fig. 1(b). The differences of these peaks between nonmagnetic and magnetic impurities are clear near the gap edges, suggesting strong dependence on coherent factors due to impurities, as well as on DOS contour of the clean system.[27,30] For nonmagnetic impurity [Fig. 6(a)], the peaks are much more sharper. This sensitivity of peaks around $(\pm\pi,0)$ is also proposed by Ref. 25, and is expected to be practically observed in the experiments. Moreover, a large peak appears around Γ [blue arrows in (Fig. 6(b)]. This suggests that the magnetic impurity's ability to localize the quasiparticle is weaker than that of the nonmagnetic one. Around (0,0), there is also a contribution originating from the homogeneous background. The mixture of such a signal makes the peak around (0,0) is not a good experimental observable to provide useful information. However, if the sample is large so that the signal from the homogeneous background has a much narrower width than the size of the electron or hole pockets, the peak at Γ can still provide a useful reference.

B. Effect of sign change

The $s_{x^2y^2}$ pairing differs from the conventional s-wave pairing that it changes sign in the BZ. To investigate the physical consequence of this effect, we artificially prohibit this sign change by letting $\Delta_1(k_x,k_y)=\Delta_2(k_x,k_y)=|\Delta_0\cos k_x\cos k_y|$ in Eq. (1). This may not correspond to any realistic physical system, but can reveal, by comparison, the effects of the sign change of the order parameter. We show the profile of $\delta\rho(\mathbf{q})$ in Fig. 7. The most observable feature is that, contrary to the sign-change case, the inter-

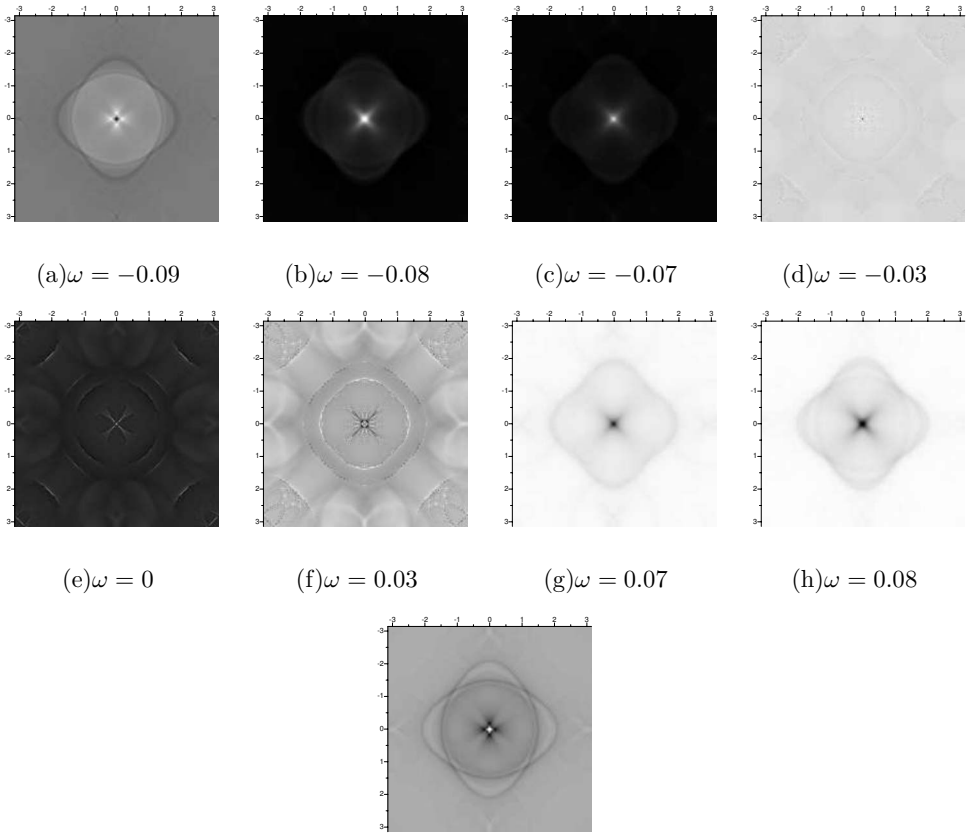

(a)$\omega = -0.09$ (b)$\omega = -0.08$ (c)$\omega = -0.07$ (d)$\omega = -0.03$

(e)$\omega = 0$ (f)$\omega = 0.03$ (g)$\omega = 0.07$ (h)$\omega = 0.08$

(i)$\omega = 0.09$

FIG. 10. The same with Fig. 9, but for magnetic impurity.

pocket peak around the M point is now sharper for the magnetic impurity.

C. QPI in other pairing symmetry

We briefly discuss the $d_{x^2-y^2}$ pairing symmetry as an example of a case with gapless nodal quasiparticles. The energy contours and interference patterns are plotted in Figs. 8–10. Besides the robust intrapocket scattering around Γ and the impurity-type sensitive peaks near $(\pm\pi,0)$ and $(0,\pm\pi)$, the most specific feature is the finite DOS within the pseudogap $\omega \in (-0.05, 0.05)$, giving rise to small but finite QPI in this region, as can be seen in (e)–(g) of Figs. 9 and 10. This originates from the intrahole pocket scattering. When $|\omega| \to 0$, the QPI concentrates on the diagonal directions as expected from the band structures in Fig. 8.

D. Analytical analysis

This section is hoped to provide a simple understanding of the above results for the two-band model. From our analysis, one can see that the features of QPI are mostly determined by (1) the density of states in k space at both $\mathbf{k}$ and $\mathbf{k}+\mathbf{q}$ and (2) the sign-changing structure of the superconducting order parameter. It is also shown that some details of the numerical results, such as the domination of the intraorbital impurity scattering over the interorbital impurity scattering in QPI, are due to the topological structure of the Bloch wave function, the importance of which has been emphasized in Ref. 49.

The two-orbital Hamiltonian can be diagonalized by a unitary transformation

$$U^{\dagger}(\mathbf{k})\begin{pmatrix} \epsilon_x(\mathbf{k}) & \epsilon_{xy}(\mathbf{k}) \\ \epsilon_{xy}(\mathbf{k}) & \epsilon_y(\mathbf{k}) \end{pmatrix} U(\mathbf{k}) = \begin{pmatrix} \epsilon_1(\mathbf{k}) & 0 \\ 0 & \epsilon_2(\mathbf{k}) \end{pmatrix}, \quad (11)$$

where

$$U = \begin{pmatrix} \cos(\theta_{\mathbf{k}}/2) & -\sin(\theta_{\mathbf{k}}/2) \\ \sin(\theta_{\mathbf{k}}/2) & \cos(\theta_{\mathbf{k}}/2) \end{pmatrix}, \quad (12)$$

and $\tan(\theta_{\mathbf{k}}) = \frac{2\epsilon_{xy}(\mathbf{k})}{\epsilon_x(\mathbf{k})-\epsilon_y(\mathbf{k})}$. The exact calculation of the T matrix is possible, however, a handy approximation for the T matrix will be applied and will reveal the physics more clearly. Practically we can numerically verify that for the strength of impurity in this work (V_0=0.4), the first order expansion in Eq. (4) is sufficiently precise (with error less than 2%). In the following, we safely take $T=V$. Throughout this work we have taken the orbital representation, and therefore in the orbital basis, the impurity Hamiltonian takes simple forms as Eq. (8) and (9). However, one may interested in the band representation if one wants to separate intrapocket and interpocket effects. One can use the unitary transform to obtain the band representation from the orbital representation. In the

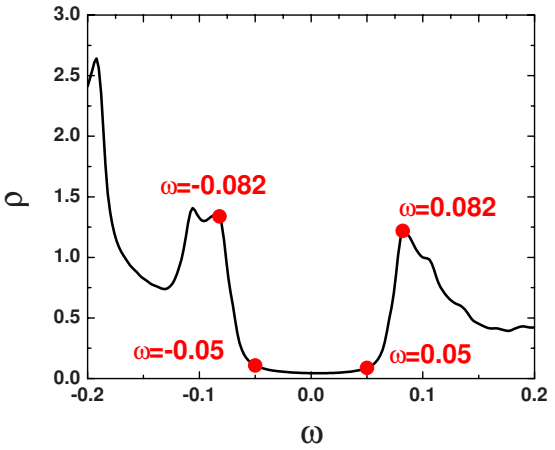

FIG. 11. (Color online) Bulk density of states ρ for five-orbital model with $s_{x^2y^2}$ pairing as a function of ω, Δ_0=0.1 and no impurities. The energy broadening width δ=0.002.

band basis, the V matrix for intraorbital impurity is in the following **k**-dependent form

$$V(\mathbf{k},\mathbf{k}') = \begin{pmatrix} \cos\left(\frac{\theta_{\mathbf{k}}-\theta_{\mathbf{k}'}}{2}\right) & \sin\left(\frac{\theta_{\mathbf{k}}-\theta_{\mathbf{k}'}}{2}\right) \\ -\sin\left(\frac{\theta_{\mathbf{k}}-\theta_{\mathbf{k}'}}{2}\right) & \cos\left(\frac{\theta_{\mathbf{k}}-\theta_{\mathbf{k}'}}{2}\right) \end{pmatrix} \otimes \begin{pmatrix} V_0 & 0 \\ 0 & \pm V_0 \end{pmatrix}, \tag{13}$$

where the upper (lower) sign is for the magnetic (nonmagnetic) impurity, as in Eqs. (8) and (9). The induced Green's function in Eq. (3) can now be transformed to the band representation. After a lengthy but straightforward calculation, we obtain

$$\delta\rho(\mathbf{q}) = [P_1(\mathbf{k},\mathbf{q}) + P_2(\mathbf{k},\mathbf{q})]V_0 \cos^2\left(\frac{\theta_{\mathbf{k}}-\theta_{\mathbf{k}+\mathbf{q}}}{2}\right) + [Q_1(\mathbf{k},\mathbf{q}) + Q_2(\mathbf{k},\mathbf{q})]V_0 \sin^2\left(\frac{\theta_{\mathbf{k}}-\theta_{\mathbf{k}+\mathbf{q}}}{2}\right), \tag{14}$$

where P_i and Q_i denote the contributions from *intrapocket* and *interpocket* scattering respectively, and take the form

$$P_{1(2)}(\mathbf{k},\mathbf{q}) = \frac{(\omega+\epsilon_{1(2)}(\mathbf{k}))(\omega+\epsilon_{1(2)}(\mathbf{k}+\mathbf{q})) \pm \Delta(\mathbf{k})\Delta(\mathbf{k}+\mathbf{q})}{(\omega^2-\Delta(\mathbf{k})^2-\epsilon_{1(2)}(\mathbf{k})^2)(\omega^2-\Delta(\mathbf{k}+\mathbf{q})^2-\epsilon_{1(2)}(\mathbf{k}+\mathbf{q})^2)},$$

$$Q_{1(2)}(\mathbf{k},\mathbf{q}) = \frac{(\omega+\epsilon_{1(2)}(\mathbf{k}))(\omega+\epsilon_{2(1)}(\mathbf{k}+\mathbf{q})) \pm \Delta(\mathbf{k})\Delta(\mathbf{k}+\mathbf{q})}{(\omega^2-\Delta(\mathbf{k})^2-\epsilon_{1(2)}(\mathbf{k})^2)(\omega^2-\Delta(\mathbf{k}+\mathbf{q})^2-\epsilon_{2(1)}(\mathbf{k}+\mathbf{q})^2)}, \tag{15}$$

where subscript 1 means the electron band and 2 means the hole band. The denominators simply give the density of states at both **k** and **k**+**q**; the numerators are the coherence factors that depend on the structure of the superconducting order parameter. The intensity of QPI thus comes from the minima of the denominators. Around the coherence peak, we have $\omega \sim |\Delta(k_f)|$, and therefore the major contribution comes from **k**'s that lie on the FS. If one thinks of the QPI intensity as a function of **q**, then the peaks should appear where we can have $\epsilon_i(\mathbf{k}) \sim \epsilon_i(\mathbf{k}+\mathbf{q}) \sim 0$. This explains why the "bright rings" in our numerical figures should take the same shape (but doubled in size) as the electron pockets. The numerators also play important roles: around the coherence peak we have $\omega \sim \pm\Delta(k_f)$, and on the energy contour $\epsilon_i(k) \sim 0$, the

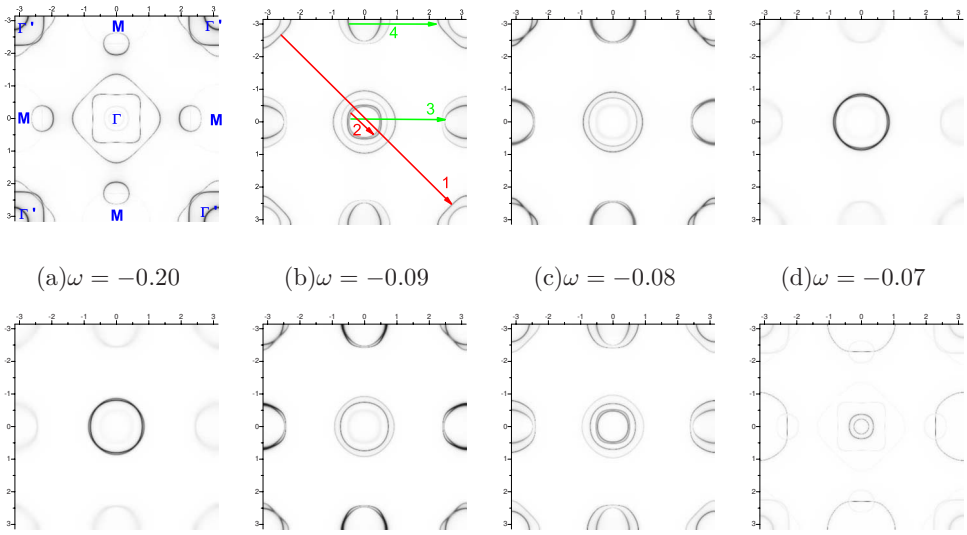

(a)$\omega = -0.20$ (b)$\omega = -0.09$ (c)$\omega = -0.08$ (d)$\omega = -0.07$

(e)$\omega = 0.07$ (f)$\omega = 0.08$ (g)$\omega = 0.09$ (h)$\omega = 0.20$

FIG. 12. (Color online) The spectral function $\mathcal{A}(\mathbf{k},\omega)$ in the unfolded Brillioun zone, for five-orbital model with Δ_0=0.1. Darker regions correspond to larger values of $\mathcal{A}$ hence larger DOS in **k** space.

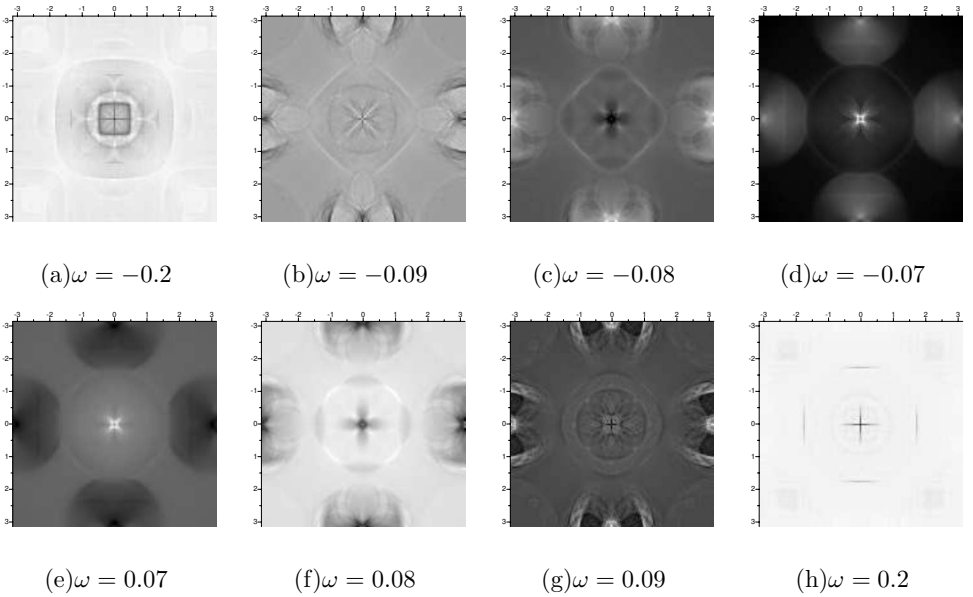

(a)$\omega=-0.2$ (b)$\omega=-0.09$ (c)$\omega=-0.08$ (d)$\omega=-0.07$

(e)$\omega=0.07$ (f)$\omega=0.08$ (g)$\omega=0.09$ (h)$\omega=0.2$

FIG. 13. $\delta\rho(\mathbf{q})$ for five-orbital model, nonmagnetic impurity with intraorbital scattering, V_0=0.4. A 160×160 lattice in $\mathbf{k}$ space is used in numerical integration of Eq. (5) and the energy broadening width δ=0.001.

magnetic impurity contribution is almost zero if $q\sim(\pi,0)$ for the sign-changing s-wave ($\Delta(\mathbf{k})=-\Delta(\mathbf{k}+\mathbf{q})$). The opposite is true if Δ does not change sign: the contribution by magnetic impurity is now much larger than that by nonmagnetic impurity. Furthermore, at $q\sim0$ the contribution by magnetic impurity is much larger than the nonmagnetic impurity. These are consistent with our numerical results and previous theoretical argument.[25]

Now let us turn to the interorbital case. After the same process, one obtains

$$V(\mathbf{k},\mathbf{k}')=\begin{pmatrix}\cos\left(\frac{\theta_{\mathbf{k}}+\theta_{\mathbf{k}'}}{2}\right) & \sin\left(\frac{\theta_{\mathbf{k}}+\theta_{\mathbf{k}'}}{2}\right)\\ -\sin\left(\frac{\theta_{\mathbf{k}}+\theta_{\mathbf{k}'}}{2}\right) & \cos\left(\frac{\theta_{\mathbf{k}}+\theta_{\mathbf{k}'}}{2}\right)\end{pmatrix}\otimes\begin{pmatrix}V_0 & 0\\ 0 & \pm V_0\end{pmatrix}. \tag{16}$$

The result is

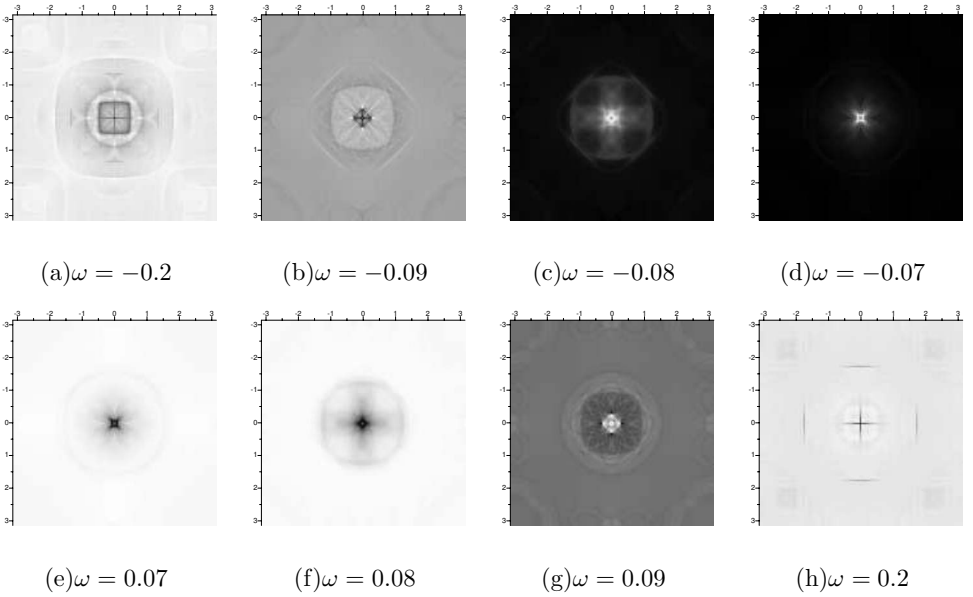

(a)$\omega=-0.2$ (b)$\omega=-0.09$ (c)$\omega=-0.08$ (d)$\omega=-0.07$

(e)$\omega=0.07$ (f)$\omega=0.08$ (g)$\omega=0.09$ (h)$\omega=0.2$

FIG. 14. Same as Fig. 13 but for magnetic impurity, V_0=0.4.

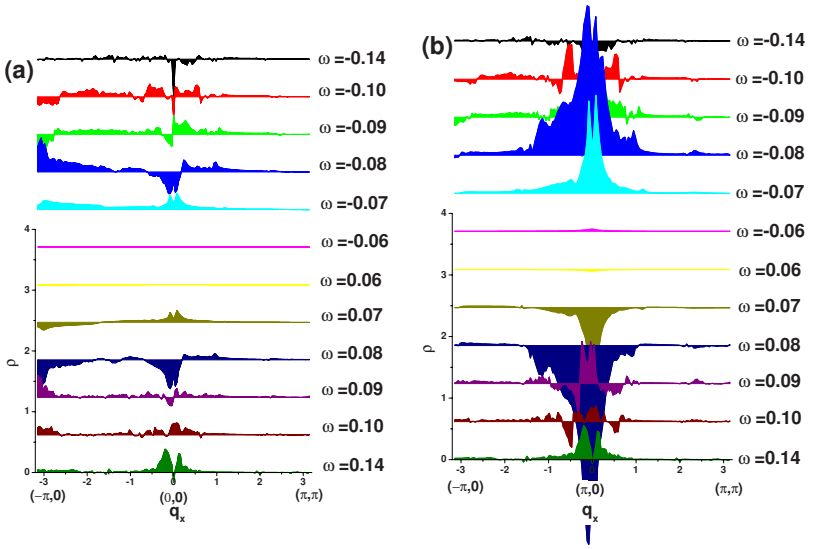

FIG. 15. (Color online) Profiles of $\delta\rho(\mathbf{q},\omega)$ along $\mathrm{M}\rightarrow\Gamma\rightarrow\Gamma'$ for (a) nonmagnetic impurity and (b) magnetic impurity in five-orbital model.

$$\delta\rho(\mathbf{q}) = [P_1(\mathbf{k},\mathbf{q}) + P_2(\mathbf{k},\mathbf{q})]V_0\frac{\cos(\theta_{\mathbf{k}}) + \cos(\theta_{\mathbf{k+q}})}{2} + [Q_1(\mathbf{k},\mathbf{q}) + Q_2(\mathbf{k},\mathbf{q})]V_0\frac{\cos(\theta_{\mathbf{k}}) - \cos(\theta_{\mathbf{k+q}})}{2}, \tag{17}$$

In our numerical section we pointed out that the interorbital contribution is much smaller than the intraorbital one. The reason lies in the structure of the function of θ_k as a function of $\mathbf{k}$. Here is a simple demonstration: in the above equation, we can see that the factor $\cos(\theta_k)$ changes fast, while the functions P and Q remain almost constants when $\mathbf{k}$ is moving along the FS. And from Ref. 49 we learned that on the two hole pockets FS, the function θ_k changes from 0 to 4π, and the θ's on the two electron pockets differ from each other by an angle of π. This tells us that the integration of $\cos(\mathbf{k})$ around the FS is zero, thus making the interorbital QPI intensity very small, which confirms what is seen in Fig. 3. This is not surprising since the intraorbital nesting in the given band structure is significant.

III. FIVE-ORBITAL MODEL AND NUMERICAL RESULTS

A better fit to the local-density approximation band structure in iron-based superconductors is given by a five orbital proposed in Ref. 50. To investigate the model-dependence of the scattering patterns, we now perform all the above calculations employing this five-orbital model augmented by an intraorbital $s_{x^2y^2}$ pairing symmetry.

In Fig. 11, we show the bulk DOS for the clean system. The coherence peaks appear at ± 0.082 and the system is fully gapped within $\sim(-0.05, 0.05)$. In Fig. 12, we plot the spectral function $\mathcal{A}(\mathbf{k},\omega)$ in the unfolded Brillioun zone, where the energy contours and their weight can be clearly seen. In Figs. 13 and 14, we plot the interference pattern $\delta\rho(\mathbf{q})$ for nonmagnetic and magnetic impurities, respectively. Their profiles in the direction $\mathrm{M}\rightarrow\Gamma\rightarrow\Gamma'$ are plotted in Fig. 15. Finally, for comparison, we also plot the results for order parameter without sign change in Fig. 16.

It is clear that the QPI in the five orbital model is quite different from that in the two orbital model. This major difference comes from the distribution of density of states at the Fermi surfaces. For example, compared with the QPI in the two-orbital model, scattering around Γ now has its origin in the intrapocket scattering within the hole pockets—in the two orbital model it originates from intraelectron pocket scattering. The density of states is higher in the electron than in the hole pockets in the two band model. The opposite is true in the five orbital model. Another clear difference is that due to the existence of additional orbitals, there exist square shaped profiles in Figs. 13(b) and 13(c) which correspond to the scattering process labeled by arrow 1 in Fig. 12(b); and the circle shaped profile in Fig. 13(d) corresponds to arrow 2. These features are absent in the two orbital model.

However, there are also common features in both models. The broad and large peaks at $\mathbf{q}=(0,0)$ for magnetic impurity appear in both models. More importantly, the $(\pm\pi,0)/(0,\pm\pi)$ sensitiveness on magnetic or nonmagnetic impurity, and sign change remains the same. For example, when Δ changes sign, the peak around $\mathbf{q}=(\pm\pi,0)/(0,\pm\pi)$ for nonmagnetic impurity [Fig. 15(a)] disappears in the case of a magnetic impurity [Fig. 15(b)]. On the contrary, when Δ does *not* change sign (Fig. 16), the peak at $(\pm\pi,0)/(0,\pm\pi)$ is related to magnetic impurity. The sensitiveness of the interference pattern around $(\pm\pi,0)/(0,\pm\pi)$ corresponds to the interpocket scattering labeled by arrows 3 and 4 in Fig. 12(b) and has been explained explicitly in the two-orbital model. Equations (14) and (15) and the arguments following them do not depend on the number of bands and therefore these features are rather universal. Moreover, the $(\pm\pi,0)/(0,\pm\pi)$ sensitiveness on the order parameter sign change (Fig. 16) is quite similar with the two-orbital model.

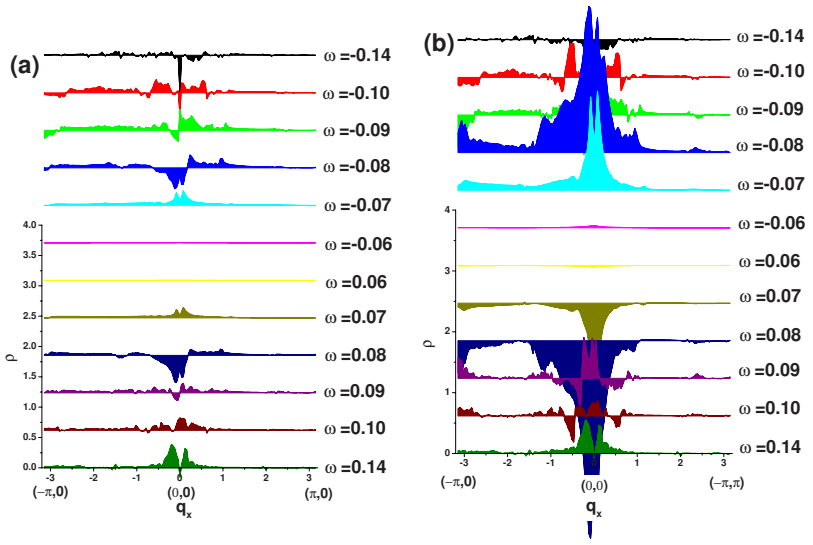

FIG. 16. (Color online) Same as Fig. 15 but for the case without sign change of Δ.

IV. CONCLUSION

In summary, we have investigated in detail the structures of the QPI in iron-based superconductors within the current available two orbital and five orbital models. The results obtained here suggest that the QPI can be used to determine the band structure and orbital degrees of freedom in these materials and can also provide evidence of the SC pairing symmetries. In this calculation, we have ignored possible three dimensional effects, more relevant for the 122 materials.[51,52] The physics associated with the third dimension and possible competing orders or coexistence states will be addressed in the future.

ACKNOWLEDGMENTS

J.P.H. and B.A.B. thank Dunghai Lee for useful discussions. J.P.H., Y.Y.Z., W.F.T., X.T.Z., K.J.S., and C.F. were supported by the NSF under Grant No. PHY-0603759.

[1] Y. Kamihara, T. Watanabe, M. Hirano, and H. Hosono, J. Am. Chem. Soc. **130**, 3296 (2008).
[2] H. Takahashi, K. Igawa, K. Arii, Y. Kamihara, M. Hirano, and H. Hosono, Nature (London) **453**, 376 (2008).
[3] G. F. Chen, Z. Li, D. Wu, G. Li, W. Z. Hu, J. Dong, P. Zheng, J. L. Luo, and N. L. Wang, Phys. Rev. Lett. **100**, 247002 (2008).
[4] X. H. Chen, T. Wu, G. Wu, R. H. Liu, H. Chen, and D. F. Fang, Nature (London) **453**, 761 (2008).
[5] H.-H. Wen, G. Mu, L. Fang, H. Yang, and X. Zhu, EPL **82**, 17009 (2008).
[6] K. Seo, B. A. Bernevig, and J. Hu, Phys. Rev. Lett. **101**, 206404 (2008).
[7] I. I. Mazin, D. J. Singh, M. D. Johannes, and M. H. Du, Phys. Rev. Lett. **101**, 057003 (2008).
[8] F. Wang, H. Zhai, Y. Ran, A. Vishwanath, and D.-H. Lee, Phys. Rev. Lett. **102**, 047005 (2009).
[9] C. Fang, H. Yao, W.-F. Tsai, J. P. Hu, and S. A. Kivelson, Phys. Rev. B **77**, 224509 (2008).
[10] T. Yildirim, Phys. Rev. Lett. **101**, 057010 (2008).
[11] Q. Si and E. Abrahams, Phys. Rev. Lett. **101**, 076401 (2008).
[12] F. Ma, Z.-Y. Lu, and T. Xiang, Phys. Rev. B **78**, 224517 (2008).
[13] C. Xu, M. Muller, and S. Sachdev, Phys. Rev. B **78**, 020501(R) (2008).
[14] H. Ding, P. Richard, K. Nakayama, T. Sugawara, T. Arakane, Y. Sekiba, A. Takayama, S. Souma, T. Sato, T. Takahashi, Z. Wang, X. Dai, Z. Fang, G. F. Chen, J. L. Luo, and N. L. Wang, EPL **83**, 47001 (2008).
[15] K. Nakayama, T. Sato, P. Richard, Y.-M. Xu, Y. Sekiba, S. Souma, G. F. Chen, J. L. Luo, N. L. Wang, H. Ding, and T. Takahashi, EPL **85**, 67002 (2009).
[16] L. Wray, D. Qian, D. Hsieh, Y. Xia, L. Li, J. G. Checkelsky, A. Pasupathy, K. K. Gomes, A. V. Fedorov, G. F. Chen, J. L. Luo, A. Yazdani, N. P. Ong, N. L. Wang, and M. Z. Hasan, arXiv:0808.2185 (unpublished).
[17] M. M. Parish, J. Hu, and B. A. Bernevig, Phys. Rev. B **78**, 144514 (2008).
[18] D. Parker, O. V. Dolgov, M. M. Korshunov, A. A. Golubov, and I. I. Mazin, Phys. Rev. B **78**, 134524 (2008).
[19] M. S. Laad and L. Craco, Phys. Rev. Lett. **103**, 017002 (2009).
[20] T. A. Maier and D. J. Scalapino, Phys. Rev. B **78**, 020514(R) (2008).
[21] W. F. Tsai, D. X. Yao, B. A. Bernevig, and J. P. Hu, Phys. Rev. B **80**, 012511 (2009).
[22] P. Ghaemi, F. Wang, and A. Vishwanath, Phys. Rev. Lett. **102**, 157002 (2009).
[23] D. Parker and I. I. Mazin, Phys. Rev. Lett. **102**, 227007 (2009).
[24] J. Wu and P. Phillips, Phys. Rev. B **79**, 092502 (2009).
[25] F. Wang, H. Zhai, and D.-H. Lee, EPL **85**, 37005 (2009).
[26] J. E. Hoffman, E. W. Hudson, K. M. Lang, V. Madhavan, H. Eisaki, S. Uchida, and J. C. Davis, Science **295**, 466 (2002).

[27] Q.-H. Wang and D.-H. Lee, Phys. Rev. B **67**, 020511(R) (2003).
[28] K. McElroy, R. W. Simmonds, J. E. Hoffman, D.-H. Lee, J. Orenstein, H. Eisaki, S. Uchida, and J. C. Davis, Nature (London) **422**, 592 (2003).
[29] K. McElroy, J. E. Hoffman, D.-H. Lee, K. M. Lang, H. Eisaki, S. Uchida, and J. C. Davis, Physica C **388**, 225 (2003).
[30] T. Pereg-Barnea and M. Franz, Phys. Rev. B **68**, 180506(R) (2003).
[31] H. D. Chen, O. Vafek, A. Yazdani, and S. C. Zhang, Phys. Rev. Lett. **93**, 187002 (2004).
[32] K. Seo, H.-D. Chen, and J. Hu, Phys. Rev. B **76**, 020511(R) (2007).
[33] K. Seo, H.-D. Chen, and J. Hu, Phys. Rev. B **78**, 094510 (2008).
[34] H. D. Chen, J. P. Hu, S. Capponi, E. Arrigoni, and S. C. Zhang, Phys. Rev. Lett. **89**, 137004 (2002).
[35] H.-D. Chen, S. Capponi, F. Alet, and S.-C. Zhang, Phys. Rev. B **70**, 024516 (2004).
[36] C. Bena, S. Chakravarty, J. Hu, and C. Nayak, Phys. Rev. B **69**, 134517 (2004).
[37] A. Ghosal, A. Kopp, and S. Chakravarty, Phys. Rev. B **72**, 220502(R) (2005).
[38] Z. Tesanovic, Phys. Rev. Lett. **93**, 217004 (2004).
[39] A. Melikyan and Z. Tesanovic, Phys. Rev. B **71**, 214511 (2005).
[40] S. Sachdev and E. Demler, Phys. Rev. B **69**, 144504 (2004).
[41] S. A. Kivelson, I. P. Bindloss, E. Fradkin, V. Oganesyan, J. M. Tranquada, A. Kapitulnic, and C. Howald, Rev. Mod. Phys. **75**, 1201 (2003).
[42] J. A. Robertson, S. A. Kivelson, E. Fradkin, A. C. Fang, and A. Kapitulnik, Phys. Rev. B **74**, 134507 (2006).
[43] D. Podolsky, E. Demler, K. Damle, and B. I. Halperin, Phys. Rev. B **67**, 094514 (2003).
[44] L. Capriotti, D. J. Scalapino, and R. D. Sedgewick, Phys. Rev. B **68**, 014508 (2003).
[45] S. Raghu, X.-L. Qi, C.-X. Liu, D. J. Scalapino, and S.-C. Zhang, Phys. Rev. B **77**, 220503(R) (2008).
[46] M. Daghofer, A. Moreo, J. A. Riera, E. Arrigoni, D. J. Scalapino, and E. Dagotto, Phys. Rev. Lett. **101**, 237004 (2008).
[47] R. Sknepnek, G. Samolyuk, Y.-B. Lee, and J. Schmalian, Phys. Rev. B **79**, 054511 (2009).
[48] The interorbital scattering in our Hamiltonain is $V(r)(c^{\dagger}_{yz}c_{xz}+c^{\dagger}_{xz}c_{yz})$ where $c^{\dagger}_{yz}$ and $c^{\dagger}_{xz}$ are creation operators of two orbitals at position r. This term already breaks the fourfold symmetry. In a rotation operation (by $\pi/2$), c_{xz} becomes c_{yz} and c_{yz} becomes $-c_{xz}$. Therefore, the term under rotation operation by $\pi/2$ changes to $-V(r)(c^{\dagger}_{yz}c_{xz}+c^{\dagger}_{xz}c_{yz})$.
[49] Y. Ran, F. Wang, H. Zhai, A. Vishwanath, and D.-H. Lee, Phys. Rev. B **79**, 014505 (2009).
[50] K. Kuroki, S. Onari, R. Arita, H. Usui, Y. Tanaka, H. Kontani, and H. Aoki, Phys. Rev. Lett. **101**, 087004 (2008).
[51] J. Zhao, D.-X. Yao, S. Li, T. Hong, Y. Chen, S. Chang, W. Ratcliff, J. W. Lynn, H. A. Mook, G. F. Chen, J. L. Luo, N. L. Wang, E. W. Carlson, J. Hu, and P. Dai, Phys. Rev. Lett. **101**, 167203 (2008).
[52] H. Q. Yuan, J. Singleton, F. F. Balakirev, S. A. Baily, G. F. Chen, J. L. Luo, and N. L. Wang, Nature (London) **457**, 565 (2009).